Geophysical Research Letters

RESEARCH LETTER
10.1029/2025GL118320

Key Points:

- Tropical cyclone structure can be divided into three parts: inner and outer cores, and far outer region based on different dominant physics
- A fast analytical model for complete tropical cyclone wind field is developed by merging wind models suitable for each region
- The new fast analytical wind model performs reliably when validated against simulations, satellite wind retrievals, and best track data

Supporting Information:

Supporting Information may be found in the online version of this article.

Correspondence to:

D. Tao,
dandantao@nju.edu.cn

Citation:

Tao, D., Nystrom, R. G., Chavas, D. R., & Avenas, A. (2026). A Fast analytical model for the complete radial structure of tropical cyclone low-level wind field. *Geophysical Research Letters*, *53*, e2025GL118320. https://doi.org/10.1029/2025GL118320

Received 20 JUL 2025
Accepted 18 DEC 2025

Author Contributions:

Conceptualization: Robert G. Nystrom, Daniel R. Chavas
Data curation: Robert G. Nystrom, Daniel R. Chavas, Arthur Avenas
Methodology: Robert G. Nystrom, Daniel R. Chavas
Writing – original draft: Robert G. Nystrom, Daniel R. Chavas
Writing – review & editing: Robert G. Nystrom, Daniel R. Chavas, Arthur Avenas

A Fast Analytical Model for the Complete Radial Structure of Tropical Cyclone Low-Level Wind Field

Dandan Tao[1], **Robert G. Nystrom**[2], **Daniel R. Chavas**[3], **and Arthur Avenas**[4,5]

[1]School of Atmospheric Sciences, Nanjing University, Nanjing, China, [2]Department of Earth, Atmosphere, and Climate, Iowa State University, Iowa, IA, USA, [3]Department of Earth, Atmospheric, and Planetary Sciences, Purdue University, Indiana, IN, USA, [4]European Space Agency (ESA), ESRIN, Frascati, Italy, [5]Laboratoire d'Océanographie Physique et Spatiale (LOPS), Ifremer, Univ. Brest, CNRS, IRD, IUEM, Plouzané, France

Abstract A tropical cyclone (TC) can generally be divided into three regions: inner core with vigorous convection, intermediate region with intermittent convection, and far outer region with less convective activity. The different physics in these three regions suggest correspondingly different wind structure models. In this study, we combine the inner-core wind model from Tao et al. (2023, https://doi.org/10.1029/2023gl104583, T23), the outer wind model from Emanuel (2004, https://texmex.mit.edu/pub/emanuel/PAPERS/Energetics_Structure.pdf, E04), and a transition model of a modified Rankine vortex to create a new fast and analytical model for the complete radial structure of the TC wind field. The T23 model captures inner-core wind variation with small errors, while the E04 model reproduces the broad outer wind structure at large radii well. The new wind model combines the strengths from both T23 and E04 models without the need for statistical fitting, showing great potential in reproducing the full range of simulated and observed TC winds.

Plain Language Summary We developed a simple analytical model to represent the full wind structure of a tropical cyclone by combining three different wind models: one for the storm's inner core, one for the far outer region, and a smooth transition in between. Each part is designed to reflect the different physical processes that occur at different distances from the storm center. The inner-core model captures how winds change during storm intensification, while the outer model accurately describes the broad, low-wind areas far from the center. Together, the combined model does a good job matching both computer-simulated and real-world observations of tropical cyclone wind profiles. In addition, no statistical fitting procedure is needed, ensuring consistency across different data sets and fast implementation. This new model can help improve our understanding of storm structure and support applications like hazard prediction and storm surge modeling.

1. Introduction

Tropical cyclones (TCs) pose significant threats to coastal regions and offshore facilities. To quantify TC impacts, accurate and efficient modeling of their wind field is essential for wind risk estimation (Vickery et al., 2009; Watson & Johnson, 2004) and storm surge modeling (Jakobsen & Madsen, 2004; Lin & Chavas, 2012; Yin et al., 2021). One widely used approach involves parametric wind models, which describe the spatial distribution of winds using mathematical expressions governed by a few key parameters. Given that parametric models are relatively simple and require minimal input data, they are especially valuable in scenarios that require a large ensemble of potential wind fields. However, accurately modeling the full TC wind field including both inner core and outer wind structure, while accounting for the large possible variations in TC size and intensity remains a challenge. While the footprint of extreme winds depends principally on winds in the inner core, inland-flooding is driven by rainfall that depends strongly on the wind field structure at intermediate radii (Xi et al., 2020). Storm surge is greatly enhanced by the weaker winds at large radii that blow over a large area and across long fetch to push water toward the shore ahead of landfall (Irish et al., 2008; Wang et al., 2022). For each of these hazards, economic damages can be linked by forcing models using a parametric wind field (Gori et al., 2025). Hence, accurately representing the wind field at all radii is important for modeling TC related hazards.

There has been a great deal of effort in developing parametric wind models. Holland (1980) used a logarithmic rectangular hyperbola to fit the observed dependence of pressure on radius, and calculated the radial distribution of the wind, $V(r)$, according to the gradient wind balance. Later, Holland et al. (2010) further advanced this wind model by allowing the shape factor, B, to vary with intensity in order to better capture the variability in the wind profiles. Meanwhile, Willoughby et al. (2006) empirically derived a sectionally continuous wind profile with analytical segments patched smoothly together. However, both Willoughby et al. (2006) and Holland et al. (2010) wind models have many tunable parameters that need to be determined statistically through fitting observational data set, which often results in varying optimal parameters for different data sets.

Emanuel (2004, hereafter E04) suggested that the radial structure of TC winds is determined by different mechanisms in different regions (e.g., inner vs. outer cores), and derived models for the outer non-convective region and the inner convective region respectively, which were then asymptotically merged. This wind model (hereafter fullE04 model) requires an input for the radius of the vanishing wind (r_0), which is however not practically available in observations. Chavas et al. (2015) extended the E04 idea and developed a complete wind model combining the theoretical wind models for an inner-core convective region (Emanuel & Rotunno, 2011) and an outer region driven by subsidence (E04). This complete model for the radial wind profile is fully physics based and requires minimal inputs to reconstruct the radial wind profile. It has been shown to compare very well against observational wind profiles, especially in the outer region versus QuikSCAT data (Chavas et al., 2015, hereafter C15), and can reproduce the observed modes of wind field variability (Chavas & Lin, 2016). The C15 model provides a physical basis for a simple empirical model to predict the radius of maximum wind from outer radii (Avenas et al., 2023; Chavas & Knaff, 2022), and has been very useful for predicting historical hazards, including the historical record of U.S. peak storm surge (Gori et al., 2023), the climatology of U.S. TC inland rainfall (Xi et al., 2020), and aggregate economic damage (Gori et al., 2025). However, this complete wind model is limited by both its slow numerical (non-analytic) calculation (Chavas et al., 2016), and the fact that the inner component of the model is too limited to capture the full structural variability of the wind profile just beyond the radius of maximum wind (Tao et al., 2023).

Recently, a simple but promising inner-core empirical wind model was developed using the quasi-linear characteristics of the absolute angular momentum surface outside the radius of maximum wind (r_m) (Tao et al., 2023, hereafter T23). The inner-core wind profile can be determined by any two points on the absolute angular momentum surface (e.g., [r_m, V_m] and [$r_{17.5}$, 17.5 ms^{-1}]) through linearity. With this simple inner-core model, the wind profile variation to intensity and size is captured without fitting any data set. However, this wind model only applies to the inner-core region such that the outer wind quickly goes to zero, similar to the inner-core wind model in Emanuel and Rotunno (2011).

As suggested in the C15 complete wind field model, it is physically meaningful to use sectional wind models. In this study, we introduce a fast and simple analytical wind model, which combines the T23 inner-core wind model and an approximation of the E04 outer wind model to take advantages of the strengths from both. The proposed model is straightforward to apply, depends on only a small number of input parameters, and is capable of reproducing the complex structure of TC wind fields in both model simulations and observations. This makes the model well-suited for applications requiring efficiency, without sacrificing too much accuracy. In Section 2, we will introduce the sectional wind model derivations and the validation data sets. Section 3 is the validation of the simple wind model results against model simulations and observations. Section 4 is conclusion and discussion.

2. Methodology

2.1. Wind Models

2.1.1. Inner-Core Region: T23 Inner-Core Wind Model

The T23 model for the inner-core wind field is developed using the quasi-linear behavior of the absolute angular momentum surface beyond r_m. A key advantage of this model is that it has no empirically fitted parameters, making it both analytically transparent and easily applicable across various scenarios. Given the wind field information at r_m and at an outer radius, for example, $r_{17.5}$, the linear slope $SL_{17.5}$ can be determined by

$$SL_{17.5} = \frac{\frac{M_{17.5}}{M_m} - 1}{\frac{r_{17.5}}{r_m} - 1}, \tag{1}$$

where $M_{17.5}$ and M_m are the absolute angular momentum at $r_{17.5}$ and r_m, respectively.

With known $SL_{17.5}$, r_m and V_m, the absolute angular momentum M at a given radius r is expressed as

$$M(r) = \left[SL_{17.5}\left(\frac{r}{r_m} - 1\right) + 1\right] M_m. \tag{2}$$

Actually, there are many alternative ways to determine the slope. One approach is using the linear fit across all available radii ($r_{17.5}$, $r_{25.7}$ and r_{33}), while anchoring the fit through the known point of r_m. In this way, we are taking advantage of all available information, and the fitted wind profile should align well with all known radii. While using two outer radii and V_m, we can also estimate r_m from the T23 model. Users can flexibly adapt the application of this model to suit their specific needs.

2.1.2. Outer-Core/Transition Region: Modified Rankine

Here we introduce a modified Rankine vortex as the transition wind model between T23 and E04. The primary purpose of using a modified Rankine is to extend the region of non-zero wind and to provide a smooth connection between the two linear absolute angular momentum models (both T23 and the approximate version of E04 have linear absolute angular momentum, more details in Section 2.1.3). The wind and absolute angular momentum equations for modified Rankine vortex are given by

$$V(r) = Ar^{-\alpha}, \tag{3}$$

$$M(r) = Vr + \frac{1}{2}fr^2 = Ar^{1-\alpha} + \frac{1}{2}fr^2, \tag{4}$$

where α is a preselected shape parameter (larger α, broader wind skirt), A is solved at the first merging point (more details in Section 2.2.1), and f is the Coriolis parameter.

2.1.3. Far Outer Region: E04

The outer descending solution (Emanuel, 2004) links the radial gradient of M at the top of the boundary layer to the thermodynamics of the quiescent free troposphere in radiative-subsidence balance. The solution is given by

$$\frac{\partial M}{\partial r} = \chi \frac{(rV)^2}{{r_0}^2 - r^2} \tag{5}$$

with

$$\chi = \frac{2C_d}{w_{cool}}, \tag{6}$$

where r_0 is the outer radius where the rotational wind goes to zero, C_d is the surface drag coefficient, and w_{cool} is the magnitude of the radiative-subsidence rate in the free troposphere.

This equation has long been known to lack an analytical solution and therefore must be integrated numerically to match some known wind radius (Chavas et al., 2015). However, this requires knowing the exact value of the outer radius r_0, as it appears in the denominator of Equation 5. Previous work solves this by employing a shooting method to search for the correct r_0 that matches the known wind radius (Chavas & Emanuel, 2010; Chavas et al., 2015). Moreover, because the denominator approaches zero at r_0, the solution blows up if the equation is integrated outward toward r_0. Chavas et al. (2016) showed that this singularity disappears when the equation is integrated in nondimensional form, with r scaled by r_0 and M by M_0. However, this approach involves two numerical convergence calculations and requires several hundred lines of code to implement. Recently, Cronin (2023) also presented a method to solve the equation using polynomial representations and offered to numerically approximate the resulting power series.

Here, we resolve this longstanding issue by exploiting a simple yet overlooked physical constraint that enables a good estimate of the r_0 from the original E04 model. Specifically, if the point $[r_0, 0]$ and one wind point $[r_1, V_1]$ on the outer wind profile are known, then the average value of dM/dr between r_1 and r_0 can be determined, which yields

$$\frac{\overline{dM}}{dr} \approx \frac{M_0 - M_1}{r_0 - r_1}. \tag{7}$$

If we approximate $\frac{\partial M}{\partial r} \approx \frac{\overline{dM}}{dr}$ and substitute in for $M_0 = \frac{1}{2} f r_0^2$ in Equation 5, we arrive at a 3rd order polynomial equation for r_0:

$$\frac{1}{2} f r_0^3 + \frac{1}{2} f r_1 r_0^2 - M_1 r_0 - \left(r_1 M_1 + \chi (r_1 v_1)^2\right) = 0, \tag{8}$$

the positive real root of which is the solution for r_0. The full profile $M(r)$ follows from Equation 7:

$$M(r) = M_0 - \frac{M_0 - M_1}{r_0 - r_1}(r_0 - r). \tag{9}$$

The above approximation produces a simple solution for M that is linear in r between r_1 and r_0. This assumption aligns closely with the full E04 model that also predicts M to be nearly linear in r at all radii except at very small wind speeds near r_0 (cf. Figures 1a and 2a in Chavas & Lin, 2016).

2.2. New Wind Model With an Analytical Solution

We now illustrate the procedure for combining the three wind models described above to construct a piecewise continuous wind profile. This process involves identifying two merging points: $[r_a, V_a]$ where the inner-core T23 model transitions to the modified Rankine vortex, and $[r_b, V_b]$ where the modified Rankine vortex transitions to the far outer-region E04 model. The smooth transitions at merging points also indicate that the piecewise structure of the model is dynamically consistent and avoids artificial discontinuities.

2.2.1. Derivation

At the first merge point $[r_a, V_a]$,

$$M_a = \left[SL_{17.5} \times \left(\frac{r_a}{r_m} - 1\right) + 1\right] M_m = A {r_a}^{(1-\alpha)} + \frac{1}{2} f r_a^2. \tag{10}$$

The smooth transition between T23 model and modified Rankine model also requires

$$\frac{dM}{dr} = SL_{17.5} \times \frac{M_m}{r_m} = A(1-\alpha) {r_a}^{-\alpha} + f r_a. \tag{11}$$

Given a preselected α and observations of r_m, V_m, $r_{17.5}$ and f at the TC center, the two unknowns (A and r_a) can be solved from the above two equations.

At the second merge point $[r_b, V_b]$, the smooth transition between modified Rankine model and E04 requires

$$\frac{\partial M}{\partial r} = \chi \frac{(r_b V_b)^2}{r_0^2 - r_b^2} = A(1-\alpha) r_b^{-\alpha} + f r_b, \tag{12}$$

while the approximation in Section 2.1.3 gives

$$\frac{\partial M}{\partial r} = \chi \frac{(r_b V_b)^2}{r_0^2 - r_b^2} \approx \frac{\overline{dM}}{dr} \approx \frac{M_0 - M_b}{r_0 - r_b}, \tag{13}$$

where $M_b = r_b V_b + \frac{1}{2} f r_b^2, M_0 = \frac{1}{2} f r_0^2, V_b = A r_b^{-\alpha}$. With preselected values of χ and α as well as the parameter A obtained above, the two unknown variables (r_b and r_0) can be determined by Equations 12 and 13.

Given the routinely available records of r_m, V_m, and $r_{17.5}$, the wind profile beyond r_m then can be fully determined. Two tunable parameters (α and χ) primarily control the locations of the merging points and the wind structure in the outer and far-outer regions. In the situation of $\alpha = 1$, there exists an analytical solution from Equations 10–13, which will be presented in the next section. Numerical solution exists for $\alpha \neq 1$ (see Tao et al., 2025). It will be shown in the α sensitivity tests that $\alpha = 1$ also gives the best reconstructed wind profile when compared to simulated wind profile in the next section.

2.2.2. Analytical Solution

Here we present the analytical solution from Equations 10–13 for A, r_a, r_b and r_0 under the situation of $\alpha = 1$:

$$A = \frac{1}{2f}\left(\frac{SL_{17.5} \times M_m}{r_m}\right)^2 + M_m(1 - SL_{17.5}), \tag{14}$$

$$r_a = \frac{SL_{17.5} \times M_m}{f r_m}, \tag{15}$$

$$r_b = \frac{1}{2}\sqrt{\chi A\sqrt{\frac{2A}{f}} + \frac{A}{2f}} - \frac{1}{4}\sqrt{\frac{2A}{f}}, \tag{16}$$

$$r_0 = \frac{1}{2}\sqrt{\chi A\sqrt{\frac{2A}{f}} + \frac{A}{2f}} + \frac{3}{4}\sqrt{\frac{2A}{f}}. \tag{17}$$

Thus, the analytical wind model is defined by the following sectional functions:

$$V(r) = \left[\left(\frac{r}{r_m} - 1\right)SL_{17.5} + 1\right]\frac{M_m}{r} - \frac{1}{2}fr, r_m \le r \le r_a; \tag{18}$$

$$Ar^{-1}, r_a \le r \le r_b; \tag{19}$$

$$\frac{A - \frac{1}{2}fr_b^2}{r} + fr_b - \frac{1}{2}fr, r_b \le r \le r_0. \tag{20}$$

For the wind profile inside r_m, we simply use a linear profile given by

$$V(r) = V_m\frac{r}{r_m}, r \le r_m. \tag{21}$$

Figure 1 shows the χ sensitivity of the analytical wind model (Equations 18–21) with the inputs of V_m, r_m, $r_{17.5}$ and f values from a simulated TC wind profile (see Section 2.3.1). Variations in χ lead to differences in the far outer low-wind region of the analytical wind model, with larger χ values producing larger r_b and r_0, as described in Equations 16 and 17. According to Chavas and Lin (2016), χ is typically around unity when using the drag coefficient from Donelan et al. (2004) as both quantities C_d and w_{cool} are approximately 0.0015–0.003 and relatively constant. For simplicity, and based on the relatively good performance shown in Figure 1, we adopt $\chi = 1.5$ in the analytical wind model used in the following sections.

We also present the α sensitivity in Figure S1 in Supporting Information S1 with the same inputs of V_m, r_m, $r_{17.5}$, f and $\chi = 1.5$. The α range that can produce a reasonable wind profile is in [0.81–1.01] for these inputs. A smaller α generates slightly larger wind beyond r_a which results in slightly larger r_0. Among the sensitivity tests, the reconstructed wind profile with $\alpha = 1$ shows the best performance compared to the simulated profile. Using $\alpha = 1$ is also justified by the observational findings in Avenas et al. (2024) that for the most intense and peaked wind profiles, relative angular momentum conservation $rV = constant$ applies for radii greater than a critical radius (about 2–3 times r_m). In the following sections, we will present the results from the analytical wind model ($\alpha = 1$) with $\chi = 1.5$.

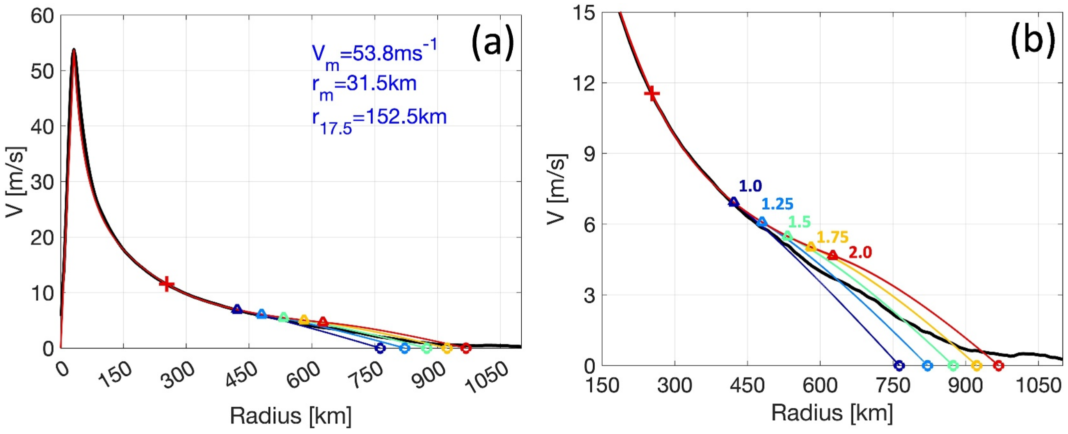

Figure 1. Wind profiles from the CM1 simulation (black) and the analytical solutions (color) with $\alpha = 1$ and $\chi \in [1.0, 2.0]$ with a 0.25 interval. The merging points (r_a, r_b) and the rotational wind vanishing point (r_0) for the analytical solution are denoted by plus, triangle and circle signs, respectively. The input values for V_m, r_m and $r_{17.5}$ are shown on the upper-right corner in (a), the corresponding enlarged outer wind profiles are shown in (b).

2.3. Validation Data Sets

2.3.1. Idealized Simulations

A three-dimensional idealized simulation was conducted using Cloud Model 1 (CM1, v21.1), initialized with a modified Rankine wind profile (exponent -0.35), featuring a surface maximum wind speed of $V_m = 15$ ms^{-1} at $r_m = 100$ km. The wind extends to $r = 200$ km, then gradually decreases to zero by $r = 500$ km. The simulation uses the moist tropical sounding from Dunion (2011), a sea surface temperature of 302.15 K and $f = 0.00005$ s^{-1}. The RRTMG radiation scheme (Iacono et al., 2008), upper-level Rayleigh damping, and a revised surface-layer scheme are adopted from the Weather Research and Forecasting Model. The model top is at 25 km, with horizontal grid spacing varying from 3 km in the inner core to 15 km at the domain edges, spanning a total of 3,300 km. The CM1 simulation provides a controlled environment with a well-resolved wind field, free from observational uncertainties, enabling accurate comparison.

2.3.2. Synthetic Aperture Radar (SAR) Wind Data

Synthetic Aperture Radar (SAR) has proven to be a valuable satellite technology for producing fine-scale, wide-swath data in the TC boundary layer under nearly all weather and all-day conditions (Mouche et al., 2017, 2019). The derived SAR products contain high-resolution estimates of the wind speed amplitude, lacking reliable information on the respective contribution from tangential and radial components, but still offering a great opportunity to investigate the TC wind profile (Avenas et al., 2024). In this study, we utilize the azimuthally averaged high-resolution (1 km) SAR data set processed by Avenas et al. (2023). In order to get a reasonable result for $SL_{17.5}$ (Tao et al., 2023), we select the SAR wind profiles with $V_m \geq 20$ ms^{-1} and available $r_{17.5}$ values. Additionally, to ensure an analytical solution, M_m needs to be less than $M_{17.5}$. After filtering, a total of 292 SAR wind profiles remain for analysis.

2.3.3. Extended Best Track

We also evaluate our analytical wind model using the Extended Best Track v2021–03–01 (Demuth et al., 2006, hereafter EBT) data for TCs in the North Atlantic and East Pacific basins. The EBT data set provides 6-hourly estimates of TC center position, intensity and wind radii (including $r_{17.5}$, $r_{25.7}$ and r_{33}) in four quadrants (northeast, northwest, southeast, southwest), as well as a single value of r_m for each TC throughout the life cycle from 1988 onward. For this study, we use data from 1988 to 2020. Wind radii are processed by averaging all available nonzero values across the four quadrants and applying a reduction factor of 0.85. This adjustment accounts for the fact that reported wind radii represent the outermost extent in each quadrant, and the average effective radius is estimated to be approximately 15% smaller (DeMaria et al., 2009). We apply the same selection

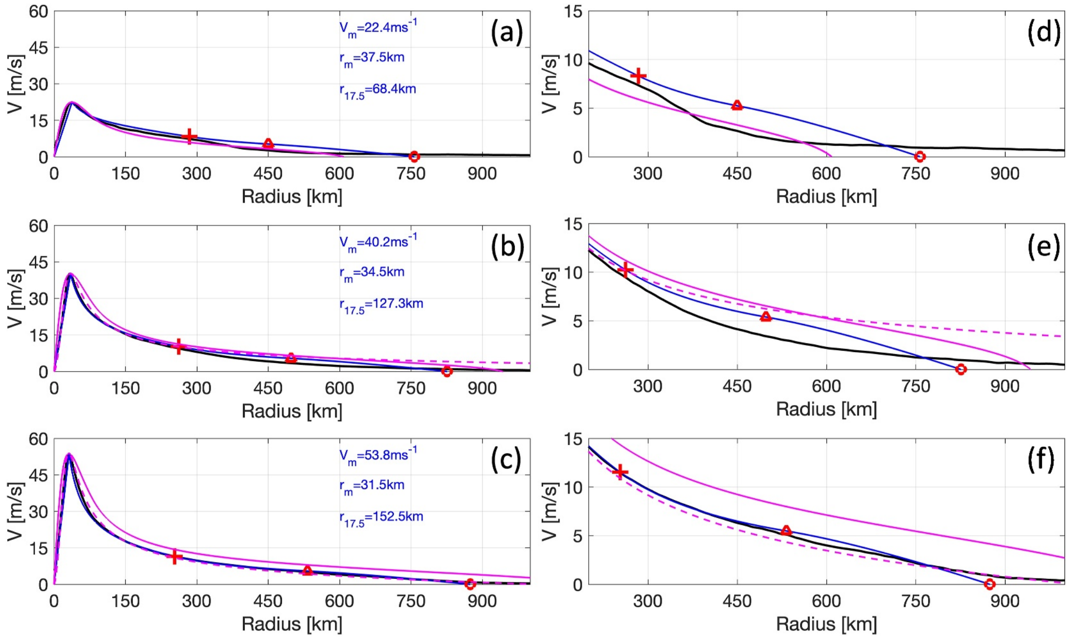

Figure 2. Wind profiles from the CM1 simulation (black), the analytical solution (blue) with $\alpha = 1$ and $\chi = 1.5$, the C15 model (solid magenta) and the fullE04 model (dashed magenta). The merging points (r_a, r_b) and the rotational wind vanishing point (r_0) from the analytical solution are denoted by plus, triangle and circle signs, respectively. The V_m, r_m and $r_{17.5}$ values are shown on the upper-right corners in (a–c), the corresponding enlarged outer wind profiles are shown in (d–f). The C15 model only takes in $[r_m, V_m]$. No dashed magenta lines in (a, d) mean that the fullE04 wind model does not have a solution for the wind profile given the inputs.

criteria to the EBT data set as in previous section, requiring $V_m \geq 20$ ms^{-1}, the availability of $r_{17.5}$ and $M_m < M_{17.5}$. The values of V_m, r_m, $r_{17.5}$ and f at TC center will be the inputs for the analytical wind model.

3. Results

3.1. Wind Model Validation Against CM1 Simulation

The azimuthally averaged 10-m tangential wind profiles for three snapshots of the simulated TC during rapid intensification (RI) are shown in Figure 2. The simulated wind profiles exhibit a rapid increase in wind speed within the inner-core region, a contraction of r_m, and an expansion of $r_{17.5}$ as the storm intensifies (Figures 2a–2c). A gradual outward expansion of the wind field in the far-outer region with intensification is also observed (Figures 2d–2f). Since the simulated TC evolves in a quiescent environment, the wind in the far-outer region is unaffected by environmental flow and can approach zero. In reality, TCs are often affected by nonzero environmental winds in the outer and far-outer regions, which can influence the observed TC wind structure.

The analytical wind model (Equations 18–21), fitted to the V_m, r_m and $r_{17.5}$ values from the CM1 simulation, effectively capture the wind structure across a range of TC intensities (Figures 2a–2c), particularly within the inner-core region. The wind decay beyond r_m and the expansion of r_0 are both reasonably well represented. The C15 model captures the overall structure of the simulated wind profiles but overestimates the wind beyond r_m in the intense TC situation (Figures 2b and 2c). In contrast, the fullE04 model (more details in Supporting Information S1) fails to provide a solution for the weak TC situation (Figures 2a and 2d), produces a nearly perfect fit for the intense TC situation (Figures 2c and 2f), and performs well in the inner core for the intermediate intensity but overestimates winds in the far-outer region (Figures 2b and 2e).

3.2. Wind Model Validation Against SAR Wind Data

Examples of individual TC azimuthally averaged total wind profiles are shown in Figure 3. The SAR-derived wind profiles extend outward up to approximately 500 km, offering detailed insight into wind structure across a range of TC sizes and intensities. The analytical wind model, using inputs of the V_m, r_m and $r_{17.5}$ values from

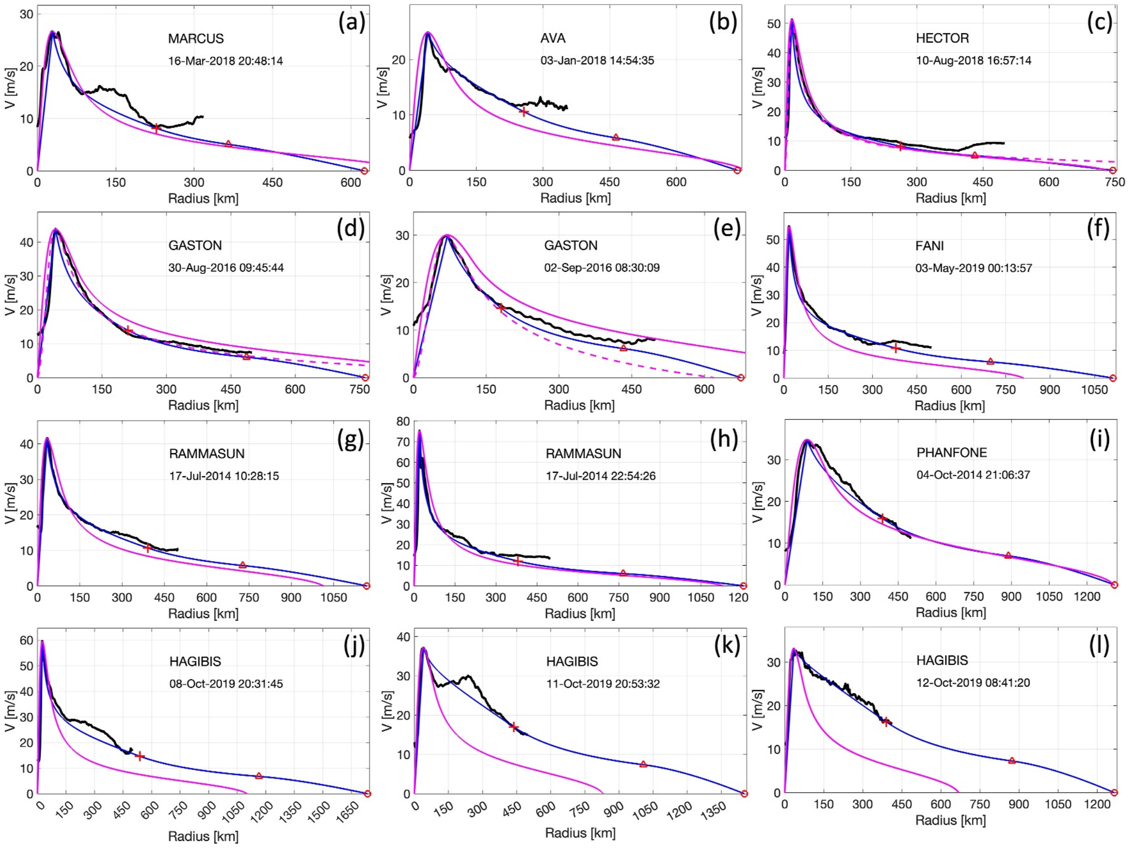

Figure 3. (a–l) Example wind profiles for TCs with different size/intensity from Synthetic Aperture Radar data set (black), the analytical wind model with $\chi = 1.5$ (blue), the C15 model (solid magenta) and the fullE04 model (dashed magenta). The merging points for the analytical wind model results are denoted by plus and triangle signs, and the rotational wind vanishing point by a circle sign. The name and time (in UTC) of the storms are also shown. Cases with no dashed magenta line mean that the fullE04 wind model does not have a solution for the wind profile given the inputs of $[r_m, V_m]$ and $\left[r_{17.5}, 17.5\ \mathrm{ms}^{-1}\right]$. The C15 model only takes in $[r_m, V_m]$. Note that the coordinates have different ranges to better exhibit the wind profiles.

SAR profiles, generally captures the wind decay beyond r_m well, despite variations among cases. However, discrepancies arise in the outer-core region, where the analytical wind model tends to underestimate wind speeds compared to SAR observations (Figures 3a–3c, 3e–3f). This is reasonable, as environmental wind in these outer regions often becomes comparable in magnitude to the TC wind. Typhoon Rammasun (2014), a rapidly intensifying TC, is well represented by the analytical wind model in both its relatively weak and intense stages (Figures 3g and 3h). Typhoon Hagibis (2019), an exceptionally large TC, is effectively captured by the model throughout its weakening phase, with size evolution reflected in changes in r_0 (Figures 3j–3l). As expected, the analytical wind model cannot capture complex structures, such as multiple-peak wind profiles due to coastal impact (Figure 3a) or secondary eyewall formation (Figure 3k).

In contrast, the C15 model fitting to $[r_m, V_m]$ generally performs well in reproducing the wind profiles except for Hagibis (Figures 3j–3l), which has been significantly underestimated. Using V_m and $\left[r_{17.5}, 17.5\ \mathrm{ms}^{-1}\right]$, the C15 model reproduces outer wind profiles that closely match the new analytical wind model results in the most cases (Figure S2 in Supporting Information S1), further confirming that the linear approximation in Section 2.1.3 is appropriate. However, the C15 model fitted to an outer radius cannot capture the inner-core structure well in some TC cases (Figures S2j–S2l in Supporting Information S1). The fullE04 model performs well for some cases (Figures 3c and 3d), underestimates winds in the outer region in others (Figure 3e) and fails to produce solutions for the rest. While using a fixed $r_0 = 1200$ km as input instead of $r_{17.5}$ in the fullE04 model following Emanuel et al. (2006), the resulting profiles tend to underestimate winds in most shown cases (Figure S2 in Supporting Information S1). Note that the inputs for the C15 model and the fullE04 model in Figure 3 and Figure S2 in Supporting Information S1 are different (see Table S1 in Supporting Information S1).

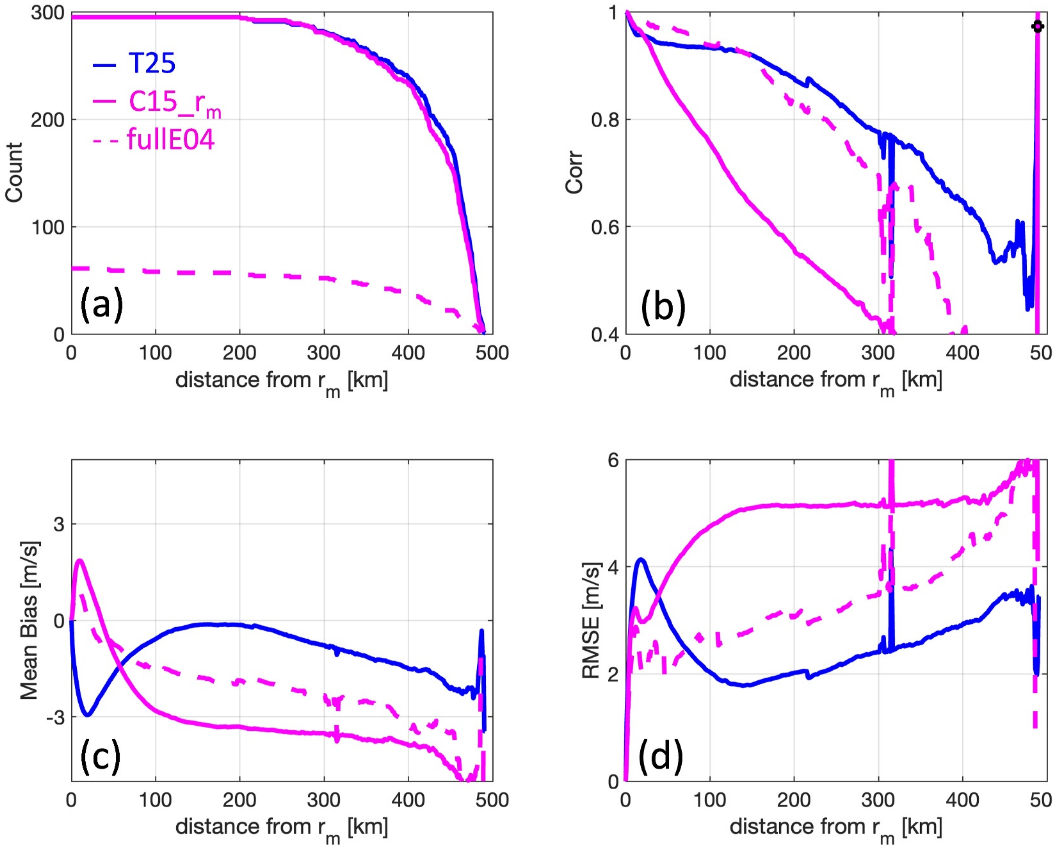

Figure 4. Results of the analytical model (blue), the C15 model (solid magenta) and the fullE04 model (dashed magenta) applied to 292 Synthetic Aperture Radar wind profiles. (a) Data count in the calculation for each radius, (b) linear correlation, (c) mean bias, and (d) root mean square error. The black circle denotes the point not passing the significance test at the 95% level. Similar to Figure 5 in Holland et al. (2010).

The overall performances of the aforementioned wind models applied to the SAR wind profiles are shown in Figure 4 and Figure S3 in Supporting Information S1. Owning to the limited SAR swath and different r_m values among SAR profiles, the radial extent of available data beyond r_m varies among profiles. The number of data points included in the statistical analysis at each radius also varies across models. For example, the fullE04 model has substantially fewer applicable cases because no solution exists for some $r_{17.5}$ values (Figure 4a). For the C15 model, the fullE04 model with a fixed $r_0 = 1200$ km and the analytical model, all 292 profiles contribute data within 200 km from r_m. However, the number of observations declines significantly beyond 250 km from r_m, and the difference among models at larger radii is due to their different r_0 values.

The correlation coefficient between the analytical model and SAR data remains above 0.8 up to approximately $\sim$250 km, though it generally decreases with increasing distance from r_m. The analytical solution has a negative bias with the largest value of -3 ms^{-1} ($\sim$10% of the mean wind magnitude at the same location) just outside r_m. The root mean square error (RMSE) maximizes with a value of 4 ms^{-1} ($\sim$14% of the mean wind magnitude at the same location) at the same distance as the bias. Among the reference models, the C15 model using $r_{17.5}$ performs better overall than that using r_m as an input, while the fullE04 model with fixed r_0 performs the worst. The comparable RMSE trends at the outer radii between the analytical model and the fullE04 model as well as the C15 model using $r_{17.5}$ (Figure 4d and Figure S3d in Supporting Information S1) provide further confirmation that the linear approximation in Section 2.1.3 is valid. Overall, the analytical wind model is well behaved, with skill exceeding the C15 and fullE04 models (Figure 4 and Figure S3 in Supporting Information S1), as well as outperforming the results reported in Holland et al. (2010) (see their Figures 5 and 6, noting that a different observational wind data set was used).

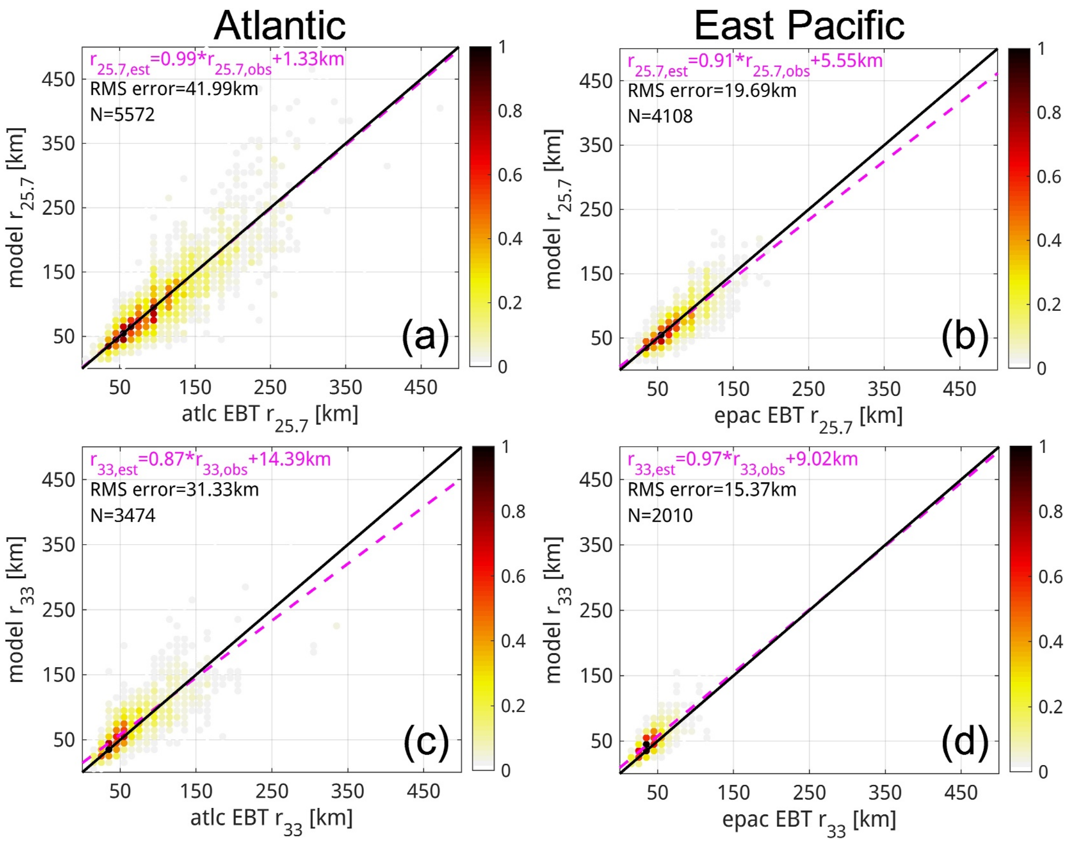

Figure 5. Estimation of $r_{25.7}$ and r_{33} using the analytical wind model with $\chi = 1.5$ and the inputs of r_m, V_m, and $r_{17.5}$ from EBT data set for (a), (c) Atlantic and (b), (d) East Pacific cyclones. Color represents for relative frequency (i.e., sample size in 10-km by 10-km bins divided by the largest sample size value of all bins); black line is the one-to-one line; and pink dashed line with equation is the linear regression. The root mean square errors (RMS error) and the numbers of data points (N) are shown on the upper-left corners.

The T23 model is developed from TCs under RI (Tao et al., 2023). To evaluate the performance of the analytical model across different scenarios, we separate the SAR profiles into RI and non-RI cases (Figure S4 in Supporting Information S1) as well as intensifying and non-intensifying cases (Figure S5 in Supporting Information S1). Interestingly, the differences between RI and non-RI, or between intensifying and non-intensifying cases, are small. Intensifying cases exhibit slightly better statistics across all three diagnostics, while RI cases show smaller overall bias and RMSE, higher correlation coefficient within 100 km from r_m, but a more rapid drop in correlation coefficient beyond ∼100 km from r_m. It is worth noting that the RI sample size is much smaller than that of the non-RI cases, which may limit the representativeness of these statistics. Overall, the weak sensitivity of the analytical model to intensification rate demonstrates its robustness for practical applications. As shown in Figure S6 in Supporting Information S1, the diagnostic statistics differ more notably between weak and strong cases. The analytical model performs better for strong cases beyond ∼100 km from r_m. Weak cases show better statistics within ∼100 km from r_m, though this should be interpreted with caution because weak cases inherently have lower wind speeds at these radii.

3.3. Wind Model Validation Against EBT

Figure 5 compares the analytical wind model estimates of $r_{25.7}$ and r_{33} against the EBT records. The model shows nearly perfect linear regression slopes for $r_{25.7}$ in the Atlantic basin (0.99) and r_{33} in the East Pacific basin (0.97). A slight overestimation is observed at smaller values for r_{33} in the Atlantic and $r_{25.7}$ in the East Pacific, while an underestimation appears at larger values, with transition points occurring near ∼100 km and ∼70 km respectively. Overall, the analytical model provides reliable estimates for both radii across the two basins, supporting the robustness and general applicability of this new wind model.

The wind values for the two merging points are shown in Figure S7 in Supporting Information S1. The V_a value has a wide range from ~ 5 ms^{-1} to ~ 28 ms^{-1} with the majority falling below 17.5 ms^{-1}. This indicates that the T23 model is suitable for representing the wind field between r_m and $r_{17.5}$ in most cases. Greater variability in V_a is seen among weaker Atlantic TCs, while the lower bound of V_a tends to increase with increasing TC intensity in both basins. The second merging point, V_b, exhibit less variability, with all values remaining below 10 ms^{-1}.

4. Conclusions and Discussion

In this study, we develop a new, fast, and fully analytical model for reconstructing the radial structure of TC low-level winds. The wind model integrates three distinct components tailored to the varying dynamical regimes of the TC wind field in three regions: the T23 model for the inner core, a transition model based on the modified Rankine vortex, and the E04 model for the far-outer region. This approach effectively captures the varying physics and wind dynamics across the inner core, intermediate, and outer regions of the storm, given the information from only two data points [r_m, V_m] and [$r_{17.5}$, 17.5 ms^{-1}]. The skill of this analytical wind model is validated against a CM1 TC simulation, SAR wind data set and EBT data set. The evaluation results demonstrate that the combined model reliably reproduces both simulated and observed wind profiles, offering a promising tool for TC structure analysis and potential operational applications. It is also worth noting that the analytical model achieves this skill without any fitting parameters and is more computationally efficient, running roughly 30 times faster than the widely used C15 model in our MATLAB tests reconstructing 292 SAR profiles. These substantial gains in both applicability and speed highlight its value for large-ensemble applications where rapid computation is essential, such as simulating thousands to millions of wind profiles in risk modeling.

The new analytical wind model's ability to capture the radial structure of TC low-level winds with no tuning highlights its robustness and applicability to a wide range of TC intensities and sizes. However, the caveat associated with this analytical wind model is its inability to represent wind profiles with multiple peaks, such as those associated with secondary eyewall formation. In addition, like many axisymmetric parametric wind models, it cannot represent TC structural asymmetries that arise due to inhomogeneities in the environment (e.g., vertical wind shear, land-sea contrast). A natural extension of this work would be to incorporate azimuthal variations by applying asymmetry coefficients, similar to the approach used in Kepert (2023).

Conflict of Interest

The authors declare no conflicts of interest relevant to this study.

Data Availability Statement

Extended Best Track data set: https://rammb2.cira.colostate.edu/research/tropical-cyclones/tc_extended_best_track_dataset/. SAR wind data set: CyclObs SAR wind products are freely available at https://cyclobs.ifremer.fr/app/. The MATLAB script for the new wind model is available on Zenodo (Tao et al., 2025): https://doi.org/10.5281/zenodo.17116429.

Acknowledgments

Dr. D. Tao is supported by the start-up funding from School of Atmospheric Sciences, Nanjing University. Dr. R. Nystrom is supported by the start-up funding from Iowa State University. Dr. D. Chavas is supported by NSF AGS 1945113 and 2431970. Dr. A. Avenas is supported by European Space Agency and Grant 4000132954/20/I-NB Marine Atmosphere eXtreme Satellite Synergy (MAXSS). Computing was conducted on the Derecho system (doi:10.5065/qx9a-pg09) provided by the NSF National Center for Atmospheric Research, sponsored by the National Science Foundation.

References

Avenas, A., Mouche, A., Knaff, J. X. C., & Chapron, B. (2024). On the tropical cyclone integrated kinetic energy balance. *Geophysical Research Letters*, *51*(16), e2024GL108327. https://doi.org/10.1029/2024GL108327

Avenas, A., Mouche, A., Tandeo, P., Piolle, J., Chavas, D., Fablet, R., et al. (2023). Reexamining the estimation of tropical cyclone radius of maximum wind from outer size with an extensive synthetic aperture radar dataset. *Monthly Weather Review*, *151*(12), 3169–3189. https://doi.org/10.1175/MWR-D-23-0119.1

Chavas, D. R., & Emanuel, K. A. (2010). A QuikSCAT climatology of tropicalcyclone size. *Geophysical Research Letters*, *37*(18), L18816. https://doi.org/10.1029/2010GL044558

Chavas, D. R., & Knaff, J. A. (2022). A simple model for predicting the tropical cyclone radius of maximum wind from outer size. *Weather and Forecasting*, *37*(5), 563–579. https://doi.org/10.1175/WAF-D-21-0103.1

Chavas, D. R., & Lin, N. (2016). A model for the complete radial structure of the tropical cyclone wind field. Part II: Wind field variability. *Journal of the Atmospheric Sciences*, *73*(8), 3093–3113. https://doi.org/10.1175/JAS-D-15-0185.1

Chavas, D. R., Lin, N., Dong, W., & Lin, Y. (2016). Observed tropical cyclone size revisited. *Journal of Climate*, *29*(8), 2923–2939. https://doi.org/10.1175/JCLI-D-15-0731.1

Chavas, D. R., Lin, N., & Emanuel, K. (2015). A model for the complete radial structure of the tropical cyclone wind field. Part I: Comparison with observed structure. *Journal of the Atmospheric Sciences*, *72*(9), 3647–3662. https://doi.org/10.1175/JAS-D-15-0014.1

Cronin, T. W. (2023). An analytic model for tropical cyclone outer winds. *Geophysical Research Letters*, *50*(11), e2023GL103942. https://doi.org/10.1029/2023GL103942

DeMaria, M., Knaff, J. A., Knabb, R., Lauer, C., Sampson, C. R., & DeMaria, R. T. (2009). A new method for estimating tropical cyclone wind speed probabilities. *Weather and Forecasting*, *24*(6), 1573–1591. https://doi.org/10.1175/2009WAF2222286.1

Demuth, J. L., DeMaria, M., & Knaff, J. A. (2006). Improvement of advanced microwave sounding unit tropical cyclone intensity and size estimation algorithms. *Journal of Applied Meteorology and Climatology*, *45*(11), 1573–1581. https://doi.org/10.1175/JAM2429.1

Donelan, M., Haus, B., Reul, N., Plant, W., Stiassnie, M., Graber, H., et al. (2004). On the limiting aerodynamic roughness of the ocean in very strong winds. *Geophysical Research Letters*, *31*(18), L18306. https://doi.org/10.1029/2004GL019460

Dunion, J. P. (2011). Rewriting the climatology of the tropical north Atlantic and Caribbean Sea atmosphere. *Journal of Climate*, *24*(3), 893–908. https://doi.org/10.1175/2010JCLI3496.1

Emanuel, K. A. (2004). Tropical cyclone energetics and structure. In E. Federovich, R. Rotunno, & B. Stevens (Eds.), *Atmospheric turbulence and mesoscale meteorology*. Cambridge University Press.

Emanuel, K. A., Ravela, S., Vivant, E., & Risi, C. (2006). A statistical deterministic approach to hurricane risk assessment. *Bulletin America Meteorology Social*, *87*(3), 299–314. https://doi.org/10.1175/BAMS-87-3-299

Emanuel, K. A., & Rotunno, R. (2011). Self-stratification of tropical cyclone outflow. Part I: Implications for storm structure. *Journal of the Atmospheric Sciences*, *68*(10), 2236–2249. https://doi.org/10.1175/JAS-D-10-05024.1

Gori, A., Lin, N., Chavas, D., Oppenheimer, M., & Xian, S. (2025). Sensitivity of tropical cyclone risk across the US to changes in storm climatology and socioeconomic growth. *Environmental Research Letters*, *20*(6), 064050. https://doi.org/10.1088/1748-9326/add60d

Gori, A., Lin, N., Schenkel, B., & Chavas, D. (2023). North Atlantic tropical cyclone size and storm surge reconstructions from 1950-Present. *Journal of Geophysical Research: Atmospheres*, *128*(5), e2022JD037312. https://doi.org/10.1029/2022JD037312

Holland, G. J. (1980). An analytic model of the wind and pressure profiles in hurricanes. *Monthly Weather Review*, *108*(8), 1212–1218. https://doi.org/10.1175/1520-0493(1980)108⟨1212:AAMOTW⟩2.0.CO;2

Holland, G. J., Belanger, J. I., & Fritz, A. (2010). A revised model for radial profiles of hurricane winds. *Monthly Weather Review*, *138*(12), 4393–4401. https://doi.org/10.1175/2010MWR3317.1

Iacono, M. J., Delamere, J. S., Mlawer, E. J., Shephard, M. W., Clough, S. A., & Collins, W. D. (2008). Radiative forcing by long-lived greenhouse gases: Calculations with the aer radiative transfer models. *Journal of Geophysical Research*, *113*(D13), D13103. https://doi.org/10.1029/2008JD009944

Irish, J. L., Resio, D. T., & Ratcliff, J. J. (2008). The influence of storm size on hurricane surge. *Journal of Physical Oceanography*, *38*(9), 2003–2013. https://doi.org/10.1175/2008JPO3727.1

Jakobsen, F., & Madsen, H. (2004). Comparison and further development of parametric tropical cyclone models for storm surge modelling. *Journal of Wind Engineering and Industrial Aerodynamics*, *92*(5), 375–391. https://doi.org/10.1016/j.jweia.2004.01.003

Kepert, J. D. (2023). A parametric model of tropical cyclone surface winds for sea and land. *Weather and Forecasting*, *38*(9), 1739–1757. https://doi.org/10.1175/WAF-D-23-0028.1

Lin, N., & Chavas, D. (2012). On hurricane parametric wind and applications in storm surge modeling. *Journal of Geophysical Research*, *117*(D9), D09120. https://doi.org/10.1029/2011JD017126

Mouche, A., Chapron, B., Knaff, J., Zhao, Y., Zhang, B., & Combot, C. (2019). Copolarized and cross-polarized SAR measurements for high-resolution description of major hurricane wind structures: Application to Irma category 5 hurricane. *Journal of Geophysical Research: Oceans*, *124*(6), 3905–3922. https://doi.org/10.1029/2019JC015056

Mouche, A., Chapron, B., Zhang, B., & Husson, R. (2017). Combined Co- and cross-polarized SAR measurements under extreme wind conditions. *IEEE Transactions on Geoscience and Remote Sensing*, *55*(12), 6746–6755. https://doi.org/10.1109/tgrs.2017.2732508

Tao, D., Nystrom, R., & Bell, M. (2023). The quasi-linear absolute angular momentum slope of tropical cyclones under rapid intensification. *Geophysical Research Letters*, *50*(16), e2023GL104583. https://doi.org/10.1029/2023GL104583

Tao, D., Nystrom, R., Chavas, D., & Avenas, A. (2025). MATLAB scripts for "A fast analytical model for the complete radial structure of tropical cyclone low-level wind field" [Software]. *Zenodo*. https://doi.org/10.5281/zenodo.17116429

Vickery, P. J., Wadhera, D., Twisdale, L. A., & Lavelle, F. M. (2009). U.S. Hurricane wind speed risk and uncertainty. *Journal of Structural Engineering*, *135*(3), 301–320. https://doi.org/10.1061/(asce)0733-9445(2009)135:3(301)

Wang, S., Lin, N., & Gori, A. (2022). Investigation of tropical cyclone wind models with application to storm tide simulations. *Journal of Geophysical Research, [Atmospheres]*, *127*(17), e2021JD036359. https://doi.org/10.1029/2021JD036359

Watson, C. C., & Johnson, M. E. (2004). Hurricane loss estimation models: Opportunities for improving the state of the art. *Bulletin America Meteorology Social*, *85*(11), 1713–1726. https://doi.org/10.1175/BAMS-85-11-1713

Willoughby, H. E., Darling, R. W. R., & Rahn, M. E. (2006). Parametric representation of the primary hurricane vortex. Part II: A new family of sectionally continuous profiles. *Monthly Weather Review*, *134*(4), 1102–1120. https://doi.org/10.1175/MWR3106.1

Xi, D., Lin, N., & Smith, J. (2020). Evaluation of a physics-based tropical cyclone rainfall model for risk assessment. *Journal of Hydrometeorology*, *21*(9), 2197–2218. https://doi.org/10.1175/JHM-D-20-0035.1

Yin, J., Lin, N., Yang, Y., Pringle, W. J., Tan, J., Westerink, J. J., & Yu, D. (2021). Hazard assessment fortyphoon-induced coastal flooding andinundation in Shanghai, China. *Journal of Geophysical Research: Oceans*, *126*(7), e2021JC017319. https://doi.org/10.1029/2021JC017319